



Diagnostic and prognostic value of amyloid PET textural and shape features: comparison with classical semi-quantitative rating in 760 patients from the ADNI-2 database

Fayçal Ben Bouallègue^{1,2} · Fabien Vauchot¹ · Denis Mariano-Goulart^{1,3} · Pierre Payoux^{2,4}

© Springer Science+Business Media, LLC, part of Springer Nature 2018

Abstract

We evaluated the performance of amyloid PET textural and shape features in discriminating normal and Alzheimer's disease (AD) subjects, and in predicting conversion to AD in subjects with mild cognitive impairment (MCI) or significant memory concern (SMC). Subjects from the Alzheimer's Disease Neuroimaging Initiative with available baseline ¹⁸F-florbetapir and T1-MRI scans were included. The cross-sectional cohort consisted of 181 controls and 148 AD subjects. The longitudinal cohort consisted of 431 SMC/MCI subjects, 85 of whom converted to AD during follow-up. PET images were normalized to MNI space and post-processed using in-house software. Relative retention indices (SUV_r) were computed with respect to pontine, cerebellar, and composite reference regions. Several textural and shape features were extracted then combined using a support vector machine (SVM) to build a predictive model of AD conversion. Diagnostic and prognostic performance was evaluated using ROC analysis and survival analysis with the Cox proportional hazard model. The three SUV_r and all the tested features effectively discriminated AD subjects in cross-sectional analysis (all $p < 0.001$). In longitudinal analysis, the variables with the highest prognostic value were composite SUV_r (AUC 0.86; accuracy 81%), skewness (0.87; 83%), local minima (0.85; 79%), Geary's index (0.86; 81%), gradient norm maximal argument (0.83; 82%), and the SVM model (0.91; 86%). The adjusted hazard ratio for AD conversion was 5.5 for the SVM model, compared with 4.0, 2.6, and 3.8 for cerebellar, pontine and composite SUV_r (all $p < 0.001$), indicating that appropriate amyloid textural and shape features predict conversion to AD with at least as good accuracy as classical SUV_r.

Keywords Alzheimer's disease · MCI · Amyloid PET · SUV_r · Texture · ADNI

Electronic supplementary material The online version of this article (<https://doi.org/10.1007/s11682-018-9833-0>) contains supplementary material, which is available to authorized users.

✉ Fayçal Ben Bouallègue
faycal.ben-bouallegue@umontpellier.fr

- ¹ Nuclear Medicine Department, Montpellier University Hospital, Montpellier, France
- ² Nuclear Medicine Department, Purpan University Hospital, Toulouse, France
- ³ PhyMedExp, INSERM – CNRS, Montpellier University, Montpellier, France
- ⁴ ToNIC, Toulouse NeuroImaging Center, Université de Toulouse, Inserm, UPS, Toulouse, France

Introduction

Considerable effort is ongoing to identify and develop reliable biomarkers of incipient Alzheimer's disease (AD) in order to target individuals who would most benefit from early treatment intervention (Jack et al. 2010), especially among subjects with mild cognitive impairment (MCI) (Petersen et al. 2013; Ellendt et al. 2016).

Positron emission tomography (PET), using ¹¹C-labeled Pittsburgh B compound (PiB) or fluorinated tracers such as ¹⁸F-florbetapir, allows in vivo visualization and quantification of cortical amyloid- β deposition, with high sensitivity and specificity compared to amyloid plaque burden at autopsy (Pontecorvo et al. 2011; Clark et al. 2012). The prognostic value of amyloid PET using fluorinated tracers (rated visually (Doraiswamy et al. 2014), semi-quantitatively (Landau et al. 2012; Ong et al. 2015), or both (Schreiber et al. 2015)) regarding cognitive decline and conversion to

AD has been highlighted in MCI patients. Its clinical impact in terms of diagnostic confidence and drug treatment has recently been demonstrated (Boccardi et al. 2016).

Semi-quantitative measures of cortical retention with respect to a reference subcortical region provide accurate and robust evaluation of amyloid burden with high test–retest reliability (Joshi et al. 2012, 2015). Although the standardized uptake value (SUV) has historically been normalized using the brainstem, pons, or whole cerebellum as reference region, evidence is growing that composite reference regions that include subcortical white matter induce less variability in sequential measurements, yielding greater power to detect A β accumulation (Chen et al. 2015; Landau et al. 2015; Brendel et al. 2015; Schwaz et al. 2017; Ben Bouallègue et al. 2017). Measures of cortical retention in small specific cortical regions are, however, limited by partial volume effect (PVE) due to the limited spatial resolution of PET scanners and image post-smoothing (Brendel et al. 2015; Schwarz et al. 2017; Gonzalez-Escamilla et al. 2016; Rullmann et al. 2016). PVE appears particularly critical when quantifying cortical tracer uptake in subjects with brain atrophy consecutive to aging and neurodegenerative disease. Another shortcoming of the SUV ratio (SUVr) pertains to the variability in SUVr estimates depending on the partitioning method used to define the cortical and subcortical regions. MRI based templates provide higher accuracy and should be preferred whenever an MR scan is available (Saint-Aubert et al. 2014), although dedicated PET templates have been developed to overcome the lack of MR data in clinical routine (Akamatsu et al. 2016; Hsiao et al. 2013).

These last decades have seen considerable development in image-based feature extraction (Lambin et al. 2012), and textural and morphological characterization of metabolic patterns in ¹⁸FDG PET has become an emerging topic in oncological nuclear medicine (Chicklore et al. 2013; Orhac et al. 2016; Buvat et al. 2015; Miwa et al. 2014; Apostolova et al. 2016). Shape assessment of computed tomography or MR images using fractal analysis has also been exploited successfully for abdominal or cerebral tumor characterization (Goh et al. 2009; Hayano et al. 2014; Smitha et al. 2015). Yet, textural and shape feature extraction has scarcely been investigated in the field of neurological PET (Klyuzhin et al. 2015), and particularly in amyloid PET. The study by Nemmi et al. (Nemmi et al. 2014) demonstrated that histogram analysis of florbetapir uptake in gray matter yields better performance than SUVr to discriminate between healthy and AD subjects in a small cross-sectional cohort. Shokouhi et al. showed that specific auto-correlation metrics measured on PiB (Shokouhi et al. 2015) and florbetapir (Shokouhi et al. 2016) PET images were more robust and better correlated with cerebrospinal fluid (CSF) markers than SUVr. Chincarini et al. proposed a global geometrical/intensity score allowing dichotomic assessment of florbetapir scans,

based on the observation that both shape and contrast of amyloid deposition differ in normal and AD subjects (Chincarini et al. 2016).

In the present study, we systematically evaluated the ability of several textural and shape parameters extracted from baseline amyloid PET to discriminate healthy and AD subjects. Their predictive value regarding AD conversion in cognitively impaired subjects was assessed against classical semi-quantitative rating using SUVr.

Materials and methods

Subjects

In this study, we used participant data from the Alzheimer's Disease Neuroimaging Initiative (ADNI), a multicenter project with approximately 50 medical centers and university sites across the United States and Canada (Petersen et al. 2010). The ADNI was launched in 2003 as a public–private partnership, led by Principal Investigator Michael W. Weiner, MD. Its primary goal was to examine how brain imaging and other biomarkers can be used to measure the progression of MCI and early AD. Determination of sensitive and specific markers of very early AD progression is expected to help researchers and clinicians to develop new treatments and monitor their effectiveness, as well as lessen the time and cost of clinical trials. A detailed description of the inclusion criteria can be found on the ADNI webpage (adni-info.org). Subjects were between 55 and 90 years old and willing and able to undergo all test procedures including neuroimaging, and all had agreed to longitudinal follow-up.

Cognitively normal participants were the control subjects in the ADNI study. They showed no signs of depression using the Geriatric Depression Rate, mild cognitive impairment or dementia. Significant memory concern (SMC) participants scored within the normal range for cognition but indicated concerns and exhibited slight forgetfulness. Early and late MCI participants reported a subjective memory concern either autonomously or via an informant or clinician. However, other cognitive domains showed no significant impairment, activities of daily living were essentially preserved, and there were no signs of dementia. AD participants met the NINCDS/ADRDA criteria for probable AD (McKhann et al. 1984; Dubois et al. 2007).

Data were downloaded from the ADNI database (adni.loni.usc.edu) and included all subjects from the ADNI-2 with available baseline florbetapir PET and cerebral MRI. Patients were recruited between January 2011 and September 2013. Seven patients for whom the automatic registration of amyloid PET with T1 weighted MRI failed were excluded. Our cross-sectional sample was made up of 181 normal controls and 148 AD subjects. Our longitudinal sample

was made up 431 subjects who were rated as SMC (104) or MCI (173 early MCI and 154 late MCI) at baseline and underwent an average clinical follow-up of 32 ± 15 months. Baseline and follow-up visits at 3, 6, and 12 months, then yearly, included complete cognitive assessment using the Alzheimer's Disease Assessment Scale–cognitive subscale (ADAS-cog). Diagnostic status at each follow-up visit was extracted from the latest available dataset ('DXSUM_PDX-CONV_ADNIALL.csv'). The last known status was the one mentioned at the time of the last visit listed in the dataset. Table 1 details the characteristics of the study population.

Image acquisition and pre-processing

Amyloid- β deposition was visualized using ^{18}F -florbetapir PET. The florbetapir images consisted of 4×5 min frames acquired at 50–70 min after injection, which were realigned, averaged, resliced to a common voxel size, and smoothed to a common resolution of 8 mm in full width at half maximum (Joshi et al. 2009) (further technical details regarding PET acquisition and pre-processing are available online at adni.loni.usc.edu/methods/pet-analysis/). Structural MR images acquired concurrently with the baseline florbetapir images (mean delay 34 ± 32 days) were used as a structural template to spatially normalize the PET images and define regions of interest (ROI) for each subject using SPM12 (Wellcome Trust Centre, London, UK). In brief, for each subject, the baseline florbetapir scan was rigidly co-registered to the baseline structural T1 weighted MR scan by maximizing normalized mutual information. The individual T1-MR scan was non-linearly co-registered to the standard Montreal Neurological Institute (MNI) space MRI template using tissue probability maps delivered with SPM. The non-linear transformation was then applied to the co-registered PET data in order to spatially normalize the PET images to the MNI space. Resulting PET data were sampled on a $135 \times 155 \times 128$ grid with cubic voxels of $1.5 \times 1.5 \times 1.5 \text{ mm}^3$ (i.e., the original resolution of the standardized images provided by the ADNI). PET image voxels were labeled according to the maximum probability tissue atlas derived from the "MICCAI 2012 grand challenge and workshop on multi-atlas labeling" and provided by Neuromorphometrics, Inc. (neuromorphometrics.com) under academic subscription.

PET data post-processing

Spatially normalized PET images were post-processed using in-house dedicated software¹ (Ben Bouallègue et al. 2017). Cortical retention indices (SUV) were computed within six

¹ The software is currently under beta-testing for routine exploitation and will soon be made available for download at: <http://scinti.edu.umontpellier.fr/recherche/logiciels-a-telecharger/>.

cortical ROIs (frontal, parietal, temporal, precuneus, anterior and posterior cingulate cortices) that were averaged to create a mean cortical SUV. Cortical SUV ratios (SUVr) were obtained by normalizing the cortical SUV with the mean uptake in a subcortical reference region. For the present study, candidate reference regions were the pons, whole cerebellum, and a composite region made up of the whole cerebellum, pons, and eroded subcortical white matter (Laudau et al. 2015; Chen et al. 2015). In the sequel, the corresponding SUVr will be respectively referred to as pontine SUVr, cerebellar SUVr, and composite SUVr. The boundaries of the three subcortical reference regions are shown in Fig. 1. White matter erosion was performed by selecting voxels which neighborhood in a 9 mm radius sphere was composed of at least 90% of white matter. For comparison, cerebellar and pontine SUVr provided by the University of California (UC), Berkeley, were retrieved from the latest available dataset on the ADNI website ('UCBERKELEYAV45_10_17_16.csv').

Textural and shape features were extracted in a volume of interest (VOI) that was built using region growing with a threshold constraint. The maximal intensity voxels in each cerebral hemisphere were chosen as seed voxels. Connected voxels that were above a given threshold were iteratively aggregated to the growing region. VOIs were constrained within a 1400 cm^3 enclosing envelope excluding extra-cerebral and sub-tentorial structures (see Fig. 1). Voxel values were normalized so that the maximal intensity inside the enclosing envelope was equal to 1. The segmentation threshold was sequentially set to 0.95 to 0 by steps of 0.05 (0.95, 0.90, 0.85...0.10, 0.05), each threshold resulting in a cerebral VOI. For each subject and each segmentation threshold, the following VOI parameters were computed.

Shape parameters

- Volume and surface of the VOI were computed on a voxel basis.
- Asphericity was defined as $A = \frac{1}{36\pi} \frac{Surf^3}{Vol^2} - 1$ with *Vol* and *Surf* the volume and surface of the VOI, and 36π the value of the ratio $\frac{Surf^3}{Vol^2}$ for a perfectly spherical VOI (Apostolova et al. 2016). This depicted how the VOI departed from a sphere.
- The convex hull of a VOI was defined as the smallest convex set of voxels containing the VOI. Convexity (sometimes referred to as solidity) was defined as the ratio of the volume of the VOI to the volume of its convex hull (El Naqa et al. 2009). Extension was defined as the ratio of the surface of the convex hull to the surface of the VOI.
- The Minkowski-Bouligand fractal dimension (FrDim) of an *m*-dimensional hypersurface Φ was defined as

Table 1 Baseline demographics, ApoE status, and ADAS-cog score in the study population

	Baseline status	Last known status	N	Follow-up (months)	Male gender	Age (years)	ApoE4 carriers	Baseline ADAS-cog
Cross-sectional cohort	Normal	—	181	—	87 (48%)	74 ± 6	52 (29%)	9 ± 5
	AD	—	148	—	86 (58%)	75 ± 8	97 (66%)*	31 ± 8*
Longitudinal cohort		Normal	113 ^(a)	25 ± 12	43 (38%)	71 ± 6	41 (36%)	9 ± 4
	SMC/MCI	MCI	233	34 ± 16*	136 (58%)*	72 ± 8	95 (41%)	14 ± 6*
		AD	85	36 ± 13*	45 (53%)*	73 ± 7	61 (72%)*†	22 ± 7**†

*: $p \leq 0.001$ vs normal. †: $p \leq 0.001$ vs MCI

(a) : among these, 93 were baseline SMC, 12 were baseline early MCI, and 8 were baseline late MCI

$dim(\Phi) = \lim_{\epsilon \rightarrow 0} \frac{\log(n_\epsilon)}{\log(1/\epsilon)}$ with n_ϵ the total number of m -dimensional boxes of side length ϵ required to cover Φ . It was evaluated by computing n_ϵ for decreasing values of ϵ using a box-counting method, then estimating the slope of $\left\{ \log\left(\frac{1}{\epsilon}\right); \log(n_\epsilon) \right\}$ through a linear regression (Falconer 1990). In two dimensions (2D, $m=2$), it stood for the fractal dimension of the surface of the VOI. In three dimensions (3D, $m=3$), it stood for the fractal dimension of the 3D radioactive distribution inside the VOI processed as a 3D hypersurface.

Textural parameters

Let D be the radioactive distribution indexed by voxel number i ($i = 1 \dots N$), and $\omega(i)$ denotes the three-dimensional 27-neighborhood of voxel i . The following features were computed inside the VOI. For the sake of simplicity, these features are referred to as ‘textural’ features in the sequel of the paper, although some of them (L^2 norm and histogram-derived parameters) do not strictly speaking reflect the spatial arrangement of adjacent voxels.

- Image L^2 norm defined as $\sqrt{\frac{\sum_i D_i^2}{N}}$, gradient L^2 norm defined as $\sqrt{\frac{\sum_i \sum_{k=x,y,z} (\nabla_k D)_i^2}{3N}}$, and Laplacian L^2 norm defined as $\sqrt{\frac{\sum_i (\Delta D)_i^2}{N}}$.
- Skewness of the voxel intensity distribution.
- Area under the curve (AUC) of the voxel intensity cumulative histogram sampled on 100 bins between 0 and 1.
- Number of local minima of D as the number of voxels such that $D_i = \min\{D_j | j \in \omega(i)\}$.
- Moran’s index $I = \frac{N}{\sum_i \sum_j w_{ij}} \frac{\sum_i \sum_j w_{ij} (D_i - \bar{D})(D_j - \bar{D})}{\sum_i (D_i - \bar{D})^2}$ and Geary’s index $C = \frac{N-1}{2 \sum_i \sum_j w_{ij}} \frac{\sum_i \sum_j w_{ij} (D_i - \bar{D})^2}{\sum_i (D_i - \bar{D})^2}$ with \bar{D} the average value of D and w a local weighting kernel based on a

distance decay function ($w_{ij} = 1/d_{ij}$ when $d_{ij} \in]0, 2[$, $w_{ij} = 0$ otherwise, with d_{ij} the distance between voxels i and j).

The isotropic gray-level co-occurrence matrix (GLCM) G was defined as (Haralick et al. 1973):

$$G_{ab} = \sum_{i=1 \dots N} \sum_{j \in \omega(i), j \neq i} \begin{cases} 1 & \text{if } \hat{D}_i = a \text{ and } \hat{D}_j = b \\ 0 & \text{otherwise} \end{cases}$$

where \hat{D} was the discrete re-sampled distribution $\hat{D} = \text{round}\{LD\}$, and where $a, b = 0 \dots L$ with L the number of gray levels (here we set $L = 50$). GLCM-based textural features were defined as follows (El Naqa et al. 2009):

- Energy: $E = \sum_a \sum_b G_{ab}^2$
- Entropy: $S = - \sum_a \sum_b G_{ab} \log(G_{ab})$
- Contrast: $T = \sum_a \sum_b (a-b)^2 G_{ab}$
- Homogeneity: $H = \sum_a \sum_b \frac{G_{ab}}{1+|a-b|}$
- Correlation: $O = \sum_a \sum_b \frac{(a-\mu_a)(b-\mu_b)}{\sigma_a \sigma_b} G_{ab}$ with $\mu_a, \mu_b, \sigma_a, \sigma_b$ respectively the marginal means and standard deviations along the a and b dimensions.

Statistical analyses

For each of the studied textural and shape parameters, the optimal segmentation threshold was defined as that maximizing the z -score between normal controls and AD patients in the cross-sectional cohort. That optimal threshold was retained for all subsequent statistical analyses and will be indicated as a subscript of the parameter in the sequel. Four parameters (surface, extension, 2D FrDim, and gradient norm) exhibited a modal distribution as a function of the segmentation threshold. Hence, maximal argument (argmax) of surface, 2D FrDim, and gradient norm, and minimal argument (argmin) of extension were investigated as potential diagnostic and prognostic markers. The

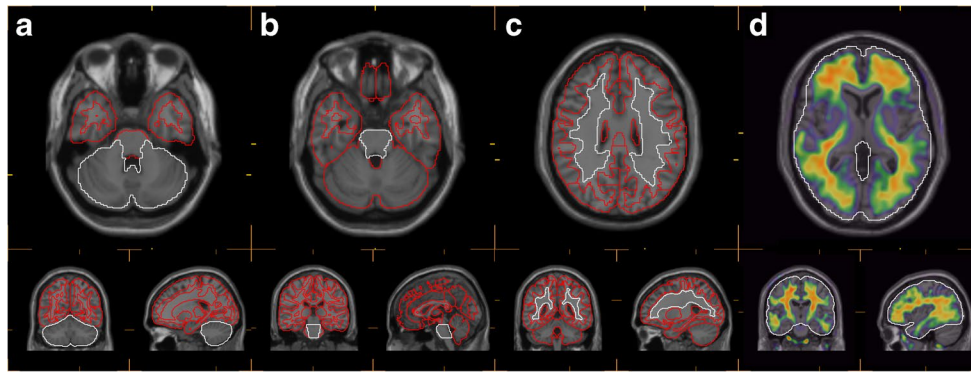


Fig. 1 Segmentation masks (in white) of the three subcortical reference regions used for SUVr computation (**a**: whole cerebellum, **b**: pons, and **c**: eroded white matter). **d**: Limits of the enclosing envelope employed for PET feature extraction

distributions of the tested parameters in normal and AD patients were compared using the Wilcoxon rank-sum test.

The diagnostic and prognostic values of the tested parameters were assessed using receiver operating characteristic (ROC) analysis with clinical status standing as the gold standard. The ROC area under the curve (AUC) stood as a measure of the global performance in discriminating normal and AD subjects, either in cross-sectional or longitudinal analysis. The optimal cutoff value was defined as that maximizing Youden's index (sensitivity + specificity - 1) in the cross-sectional cohort. Sensitivity was computed as the positivity rate in AD subjects, and specificity as the negativity rate in normal subjects. The same cutoff values were employed in cross-sectional and longitudinal analyses. Sensitivities, specificities, and accuracies were compared using McNemars's test.

A least squares support vector machine (SVM) was used to construct a predictive model of AD conversion based on textural and shape features. An SVM is a non-probabilistic binary classifier based on a set of hyperplanes that are optimized using a training dataset (Vapnik 1999). Each tested SVM implied a combination of textural and shape features. The model was trained on the cross-sectional cohort using a quadratic kernel function and validated on the longitudinal cohort. Since an exhaustive search of the optimal combination of features was not computationally possible, the best SVM was built by first finding the optimal combination of three features then adding features one by one to the model. The optimization criterion was the maximization of ROC AUC in predicting AD conversion.

The predictive value of SUVr, textural and shape features, and the SVM classifier regarding conversion to AD in the longitudinal cohort was assessed using Kaplan–Meier survival curves. Hazard ratios (HR) were adjusted using a Cox proportional hazard model including gender, age, ApoE4 status, and baseline ADAS-cog

score as explanatory covariates. For patients who did not convert to AD, survival data were considered censored from the time of the last visit on record.

A two-sided p -value ≤ 0.05 was considered statistically significant. All p -values related to parameter distributions and adjusted hazard ratios were corrected for multiple comparisons using the Dunn–Šidák correction: $p_{\text{corrected}} = 1 - (1 - p)^m$ with m the number of comparisons. All statistical computations were performed using Matlab R2013 (The Math Works, Natick, MA).

Results

Figures 2 and 3 show the distribution (inter-quartile range) of textural and shape features as a function of the VOI segmentation threshold and according to the diagnostic status. For each feature, the left panel refers to the cross-sectional cohort and distinguishes subjects in terms of baseline status (normal or AD), and the right panel refers to the longitudinal cohort and distinguishes subjects in terms of last known status (normal, MCI, or AD). The vertical dashed lines stand for the optimal threshold maximizing the z -score between normal controls and AD subjects in cross-sectional analysis. It is noteworthy that the distributions in normal and AD subjects were highly similar in both cohorts for all the tested features. As already stated, surface, extension, 2D FrDim, and gradient norm were characterized by a modal distribution in which the argument of the local extremum was sensibly different in normal and AD subjects.

Table 2 details the performance of SUVr, textural and shape features, and the SVM classifier in the cross-sectional and longitudinal analyses. Inter-quartile ranges in normal controls and AD subjects were significantly different for all the tested parameters (all $p < 0.001$ after correction for multiple comparison). Regarding SUVr, the composite reference region yielded the best performance

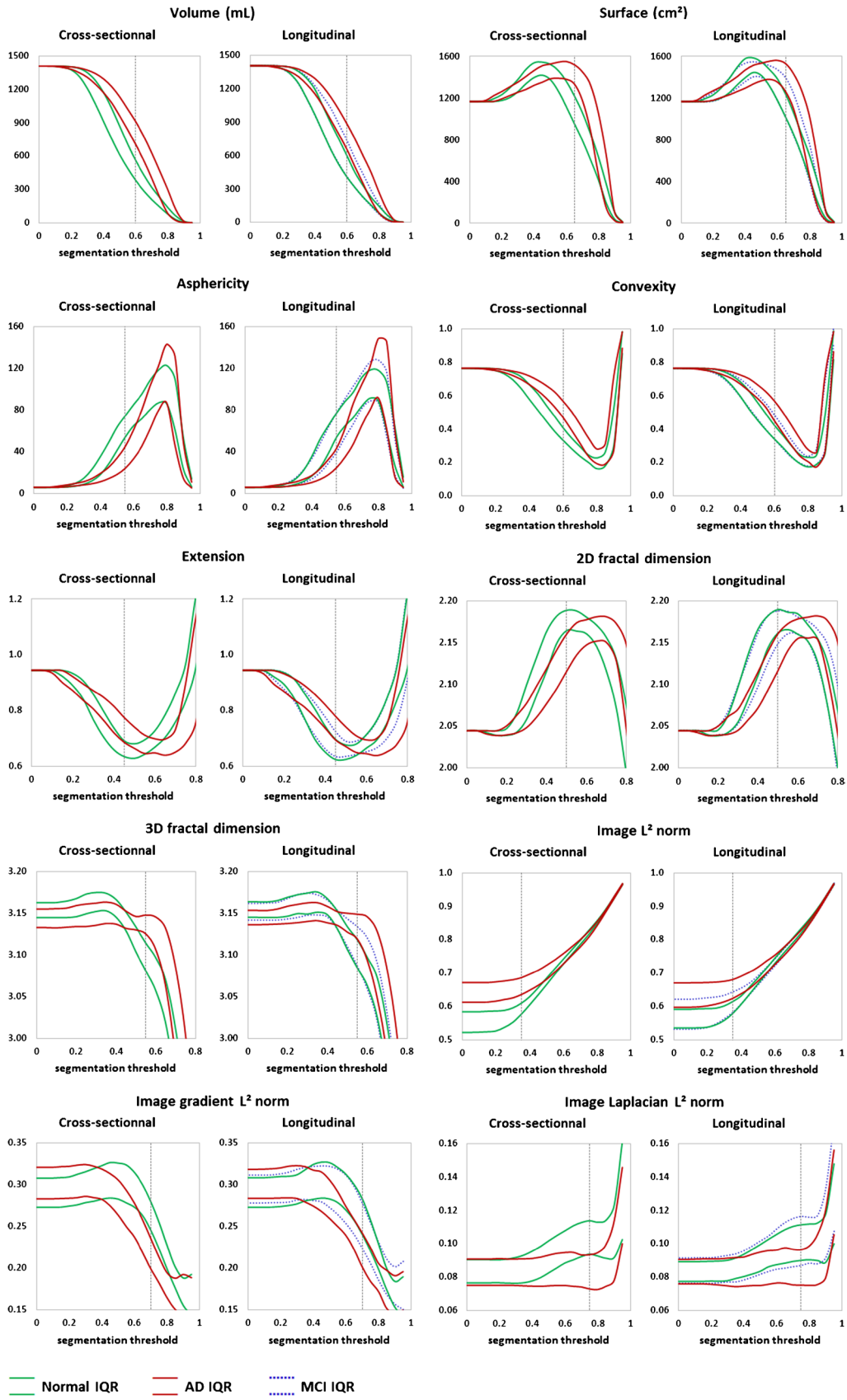


Fig. 2 Distribution of textural and shape features according to the segmentation threshold in the cross-sectional and longitudinal cohorts. The vertical dashed lines stand for the optimal threshold maximizing the z-score between normal controls and AD subjects in cross-sectional analysis. Status (normal, AD, MCI) refers to baseline status in the cross-sectional cohort and last known status in the longitudinal cohort. IQR: inter-quartile range

with ROC AUCs of 0.85 and 0.86 and accuracies of 83% and 81% in cross-sectional and longitudinal analyses respectively, and a hazard ratio for AD conversion of 7.4 (adjusted 3.8; $p < 0.001$). As quality control, cerebellar and pontine SUVr were highly correlated with those provided by UC Berkeley (Pearson's $r = 0.98$ for both SUVr, see Supplementary Fig. 1), attesting the goodness of image registration and ROI definition.

The textural and shape indices whose diagnostic performance (discrimination between normal controls and AD subjects in the cross-sectional cohort) was similar to that of composite SUVr were volume_{60%} (ROC AUC 0.84; accuracy 82%), surface_{65%} (0.84; 82%), convexity_{60%} (0.83; 82%), image norm_{35%} (0.84; 82%), skewness_{15%} (0.88; 85%), cumulative histogram AUC_{35%} (0.84; 81%), local minima_{55%} (0.85; 83%), extension argmin (0.84; 82%), and gradient norm argmax (0.83; 83%). In longitudinal analysis, the textural and shape indices whose predictive value was similar to that of composite SUVr included skewness_{15%} (AUC 0.87; 83% accuracy; adj. HR 4.0; $p < 0.001$), cumulative histogram AUC_{35%} (AUC 0.82; 80% accuracy; adj. HR 3.4; $p < 0.001$), local minima_{55%} (AUC 0.85; 79% accuracy; adj. HR 3.1; $p < 0.01$), Geary's $C_{20\%}$ (AUC 0.86; 81% accuracy; adj. HR 3.8; $p < 0.001$), and gradient norm argmax (AUC 0.83; 82% accuracy; adj. HR 4.3; $p < 0.001$).

The optimal SVM model built using the cross-sectional cohort as training dataset consisted of the combination of seven textural and shape indices: volume_{60%}, asphericity_{55%}, convexity_{60%}, histogram skewness_{15%}, surface argmax, 2D FrDim argmax, and gradient norm argmax. Its validation on the longitudinal cohort yielded a ROC AUC of 0.91 (vs 0.86 for composite SUVr, $p = 0.14$), 86% accuracy (vs 81%, $p = 0.03$), 85% sensitivity (vs 78%, $p = 0.08$), 88% specificity (vs 84%, $p = 0.20$), and a hazard ratio of 10.1 (adjusted 5.5; $p < 0.001$). Figure 4 shows the ROC curves of the three SUVr and the SVM classifier for predicting AD conversion. Figure 5 compares the predictive performance of composite SUVr and the SVM model. The scatter plot of SUVr values and SVM scores according to last known status (normal, AD, or MCI) is shown on the left. The dashed lines indicate the cutoff values for SUVr (0.88) and SVM (0). The Kaplan–Meier curves for AD conversion in the longitudinal cohort are shown on the right, according to the composite SUVr profile and SVM classification.

Figure 6 shows two examples from the longitudinal cohort for which SVM classification outperformed composite SUVr rating (A: normal subject; B: AD converter). Composite SUVr and relevant textural and shape features are detailed along with the normalcy cutoffs established by ROC analysis of the cross-sectional cohort. Cerebral VOIs corresponding to segmentation thresholds ranging from 20 to 70% are displayed on the right.

Discussion

In this study based on prospective data from the ADNI-2 cohort, we investigated to what extent the texture and shape of amyloid deposition computed on baseline florbetapir PET were characteristic of AD status and predictive of AD conversion in MCI subjects. Concurrent baseline MRI scans were available and exploited for PET data normalization in order to obtain accurate brain partitioning for SUVr measurements (Saint-Aubert et al. 2014). As expected, all three SUVr were significantly different in normal and AD subjects, in both cross-sectional and longitudinal analyses. Composite SUVr showed slightly better diagnostic and prognostic performance than cerebellar and pontine SUVr, in line with previous evidence of the superiority of SUVr accounting for white matter (Chen et al. 2015; Landau et al. 2015; Brendel et al. 2015; Ben Bouallègue et al. 2017).

Our results demonstrate that amyloid PET textural and shape analysis is feasible and yields relevant semi-quantitative markers of amyloid plaque burden. The underlying approach eliminates the need for count ratio (SUVr) computations, which is appealing on both sides of the ratio. First, on the cortical side, the method does not require the segmentation of cortical regions of interest. Cortical ROIs are usually obtained after partitioning of the registered PET data using a reference atlas. Registration inaccuracies and segmentation imperfections related to inter-individual anatomical variability have an impact on the measured cortical retention indices. Registration and segmentation are particularly critical in subjects with cortical remodeling due to aging and neurovascular or neurodegenerative disease. Ideally, PET data registration should rely on concurrent MR imaging (Saint-Aubert et al. 2014), which is often not available in routine clinical practice. Moreover, quantification of cortical ROIs inherently suffers from PVE, especially in subjects with cortical atrophy (Rullmann et al. 2016). Second, on the subcortical side, our textural and shape characterization is independent of any subcortical reference. There is currently no consensus regarding the ideal subcortical reference region. Pontine and cerebellar uptake is prone to noise and longitudinal variability due to the small size of the considered regions and their peripheral location in the PET scanner field of view (Chen et al. 2015; Landau et al.

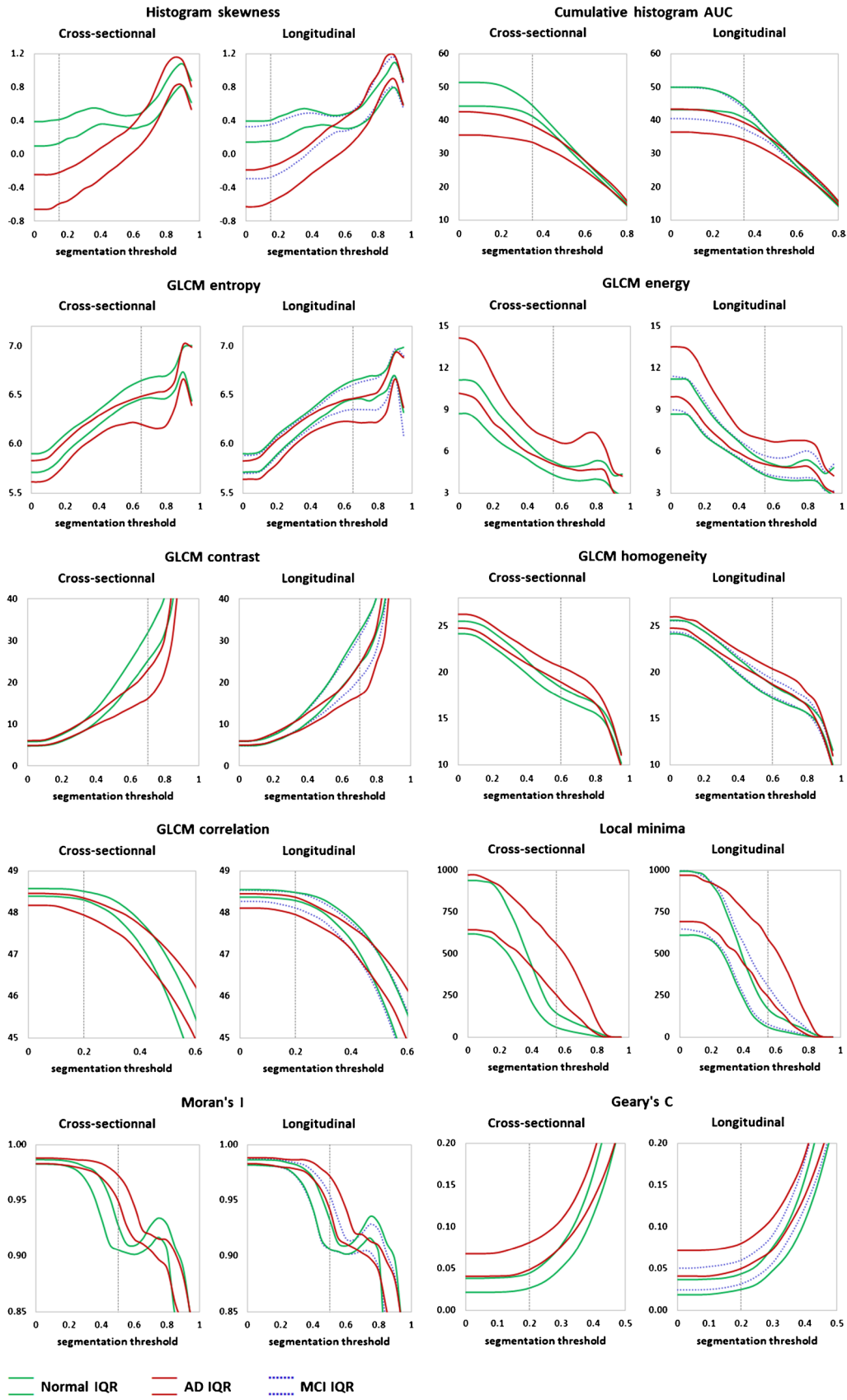


Fig. 3 Distribution of textural and shape features according to the segmentation threshold in the cross-sectional and longitudinal cohorts. The vertical dashed lines stand for the optimal threshold maximizing the z-score between normal controls and AD subjects in cross-sectional analysis. Status (normal, AD, MCI) refers to baseline status in the cross-sectional cohort and last known status in the longitudinal cohort. IQR: inter-quartile range

2015). Although composite reference regions seem to allow more robust quantification (Chen et al. 2015; Landau et al. 2015; Brendel et al. 2015; Schwaz et al. 2017), recent results tend to demonstrate that white matter uptake might not be as specific as it was thought to be (Nemmi et al. 2014).

Standard assessment of amyloid PET is based on qualitative binary reading using established interpretation criteria that are applicable to PiB and fluorinated tracers (Minoshima et al. 2016). Quantification of amyloid deposition based on count ratios may be used in addition, although its variability among tracers, scanners, and post-processing methods still requires substantial standardization effort (Klunk et al. 2015). The results presented here indicate that textural and shape analysis of cerebral tracer uptake are capable of translating visual impression into a relevant quantitative information. The validity of the proposed indices has been assessed using florbetapir images but should hold for other amyloid tracers. Indeed, although differences in pharmacokinetics and pharmacodynamics may induce variations in semi-quantitative estimations, uptake patterns are expected to be similar.

The shape indices aimed to describe the loss of gray/white matter contrast and the extension of tracer uptake to the edge of the cerebral cortex in pathological scans. These were thus characterized by a higher volume and surface, lower asphericity, higher convexity and extension, and lower 2D FrDim due to the smooth regular boundary of the cortical uptake (Fig. 6B). In negative scans, the confinement of tracer uptake to white matter with numerous concave arboreal ramifications yielded the inverse trend in the shape indices (Fig. 6A). These indices showed diagnostic and prognostic performance that was globally almost as good as that of SUVR. Of note, basic descriptors such as asphericity_{55%} and convexity_{60%} demonstrated diagnostic and prognostic accuracies and hazard ratio for AD conversion similar to those of optimal semi-quantitative rating. Although the 55% and 60% segmentation thresholds may appear limiting in the sense that they may vary in function of the tracer used or the scanner resolution, Fig. 2 clearly shows that the discriminative power of the shape parameters remained valid over a broad range of threshold values (40–70% as regards asphericity and convexity, for example). Besides, the shape parameters that exhibited a modal distribution as a function of segmentation

threshold, like surface or extension, were able to provide a pertinent global characterization of tracer uptake that was independent of any arbitrary segmentation, with excellent diagnostic and prognostic values.

Albeit broadly studied in the field of oncological PET imaging, textural features have been little investigated with regard to brain PET (and particularly amyloid PET) imaging. Textural markers of tracer uptake are known to carry subtle information that surpasses classical ROI quantification (Buvat et al. 2015). The textural parameters tested here included well-established first-order (histogram-based) and second-order (GLCM-based) parameters, as well as standard measures of spatial auto-correlation (Moran's I and Geary's C). The L^2 norm of the image and its first and second derivatives, and the number of local minima, are less usual but appear as natural markers of global heterogeneity. Histogram-based indices (skewness_{15%} and cumulative histogram AUC_{35%}) were highly correlated with the subject's status and strong markers of progression to AD, as they reflected the prevalence of high-intensity voxels in positive scans and low-intensity voxels in negative scans. This was already highlighted in (Nemmi et al. 2014) based on separate histogram analysis of gray and white matter. Consistent with the results of Shokouhi et al. (Shokouhi et al. 2016), global measures of spatial auto-correlation were relevant indicators of amyloid load distribution. Our results demonstrate their prognostic value, as Geary's C performance in longitudinal analysis was equivalent to that of composite SUVR (same AUC, accuracy, and adjusted HR).

As described in the Methods section, the image acquisition protocols of ADNI-2 were designed to ensure the consistency of PET data within and between sites, particularly in terms of spatial resolution (via post-smoothing) and signal-to-noise ratio (via injected doses, injection-to-acquisition delay, and scan duration). This standardization step was an important prerequisite for obtaining reliable shape and texture indices with minimal intra-class variability. Our results attest that such indices extracted from multi-site data carry relevant information provided that the image quality has been harmonized. PET images were spatially normalized to the MNI space for SUVR computations. For texture and shape characterization, voxel registration and labeling were also required to mask extra-cerebral activity. The lack of small cortical ROIs, however, renders the registration process and the template choice less demanding and dedicated PET templates should provide sufficiently accurate registration when MR data are not available (Akamatsu et al. 2016; Hsiao et al. 2013).

Automated multivariate data analysis tools like discriminant analysis, naïve Bayes classification, and support vector machine are powerful supervised learning techniques meant to deal with complex, high-dimensional

Table 2 Diagnostic and predictive values of SUVr, textural and shape features, and SVM classification (the SVM model included volume, asphericity, convexity, skewness, surface argmax, 2D fractal dimension argmax, and gradient norm argmax). Thresh.: optimal segmentation threshold. IQR: inter-quartile range. AUC: area under the ROC curve. Se: sensitivity (positivity rate among AD patients). Sp: specificity (negativity rate among normal patients). Ac: accuracy. PV: positive predictive value. NV: negative predictive value. HR: Cox hazard ratio (adj: adjusted on age, gender, and ApoE status, then on age, gender, ApoE status, and baseline ADAS-cog). The same cutoff values were employed in cross-sectional and longitudinal analyses

	Cross-sectional										Longitudinal									
	Thresh	Normal IQR	AD IQR †	AUC	Cutoff	Se (%)	Sp (%)	Ac (%)	AUC	Se (%)	Sp (%)	Ac (%)	PV (%)	NV (%)	HR	adj HR *				
Cerebellar SUVr	–	[0.97 1.14]	[1.24 1.48]	0.82	>1.23	76	84	81	0.84	75	82	79	43	33	7.2	5.3	4.0			
Pontine SUVr	–	[0.59 0.73]	[0.82 1.01]	0.85	>0.82	76	87	82	0.84	67 (–)	84	77 (–)	41	33	5.5	4.3	2.6 ^a			
Composite SUVr	–	[0.69 0.81]	[0.91 1.08]	0.85	>0.88	82	85	83	0.86	78	84	81	41	35	7.4	5.8	3.8			
Volume (mL)	60%	[380 561]	[702 909]	0.84	>671	79	85	82	0.81	73	84	79	40	34	5.6	4.3	3.0			
Surface (cm ²)	65%	[956 1222]	[1337 1521]	0.84	>1292	80	85	82	0.82	74	82	79	38	35	5.4	3.8	2.5 ^b			
Asphericity	55%	[55 75]	[24 45]	0.81	<47	77	85	81	0.79	78	80	79	40	34	6.5	5.1	3.5			
Convexity	60%	[0.33 0.41]	[0.47 0.57]	0.83	>0.46	76 (–)	87	82	0.81	72	86	80	42	34	5.7	4.4	3.1			
Extension	45%	[0.63 0.69]	[0.69 0.77]	0.79	>0.71	66 (–)	86	77 (–)	0.79	69	80	75	38	33	4.5	3.6	2.6 ^a			
2D fract. dim	50%	[2.16 2.19]	[2.12 2.16]	0.80	<2.16	75 (–)	81	78 (–)	0.80	74	78	76	38	33	5.3	4.2	2.9 ^a			
3D fract. dim	55%	[3.08 3.11]	[3.13 3.15]	0.81	>3.12	78	82	80	0.81	74	80	77	38	34	5.1	3.8	2.5 ^b			
Image norm	35%	[0.58 0.61]	[0.64 0.69]	0.84	>0.63	78	85	82	0.81	69	86	79	41	34	5.1	3.8	3.0			
Gradient norm	70%	[0.25 0.28]	[0.20 0.24]	0.81	<0.25	85	73 (–)	79 (–)	0.80	85	67 (–)	75 (–)	33	36	5.9	4.4	3.4			
Laplacian norm	75%	[0.09 0.11]	[0.07 0.09]	0.78 (–)	<0.09	74 (–)	77 (–)	76 (–)	0.73 (–)	68	73 (–)	71 (–)	34	31	3.7	2.9	2.6 ^a			
Skewness	15%	[0.13 0.42]	[–0.59 –0.22]	0.88	<–0.08	85	86	85	0.87	81	85	83	42	36	8.6	6.9	4.0			
Cum. hist. AUC (%)	35%	[63 68]	[51 59]	0.84	<62	82	81	81	0.82	80	80	80	38	35	6.7	5.1	3.4			
Entropy	65%	[6.46 6.65]	[6.20 6.49]	0.80	<6.51	82	67 (–)	74 (–)	0.79	85	61 (–)	71 (–)	29	38	4.3	3.3 ^a	2.9 ^b			
Energy	55%	[4.32 5.26]	[5.08 6.82]	0.81	>4.80	88	59 (–)	72 (–)	0.78	88 (+)	56 (–)	70 (–)	28	39	4.9	3.6 ^a	ns			
Contrast	70%	[25.2 31.9]	[16.1 23.0]	0.83	<24.5	81	78 (–)	80 (–)	0.81	74	75 (–)	75 (–)	33	36	4.0	2.8 ^a	ns			
Homogeneity	60%	[17.3 18.4]	[19.0 20.6]	0.84	>18.6	83	79 (–)	81	0.82	81	73 (–)	77	35	35	5.9	4.5	3.3 ^a			
Correlation	20%	[48.3 48.5]	[47.9 48.4]	0.76 (–)	<48.3	66 (–)	79	73 (–)	0.77 (–)	64 (–)	78	72 (–)	29	36	2.4	2.3 ^a	ns			
Local minima	55%	[59 144]	[252 558]	0.85	>189	84	82	83	0.85	80	79	79	37	36	6.4	4.9	3.1 ^a			
Moran's I	50%	[0.91 0.93]	[0.95 0.97]	0.83	>0.94	79	84	82	0.81	74	81	78	39	34	5.5	4.2	3.0			
Geary's C	20%	[0.03 0.04]	[0.05 0.08]	0.84	>0.04	81	75 (–)	78 (–)	0.86	86 (+)	78	81	34	40	6.9	4.8	3.8			
Argmax (surface) (%)	–	[40.9 50.7]	[52.2 62.3]	0.83	>53	74 (–)	87	81	0.79	73	85	80	41	34	5.8	4.1	3.0			
Argmin (extension) (%)	–	[44.5 55.4]	[58.2 69.7]	0.84	>57	76 (–)	87	82	0.80	75	85	81	41	35	6.3	4.9	3.2			
Argmax (2D fr. dim.) (%)	–	[49.8 60.4]	[61.0 71.4]	0.79	>61	74 (–)	82	78 (–)	0.80	66 (–)	78	73 (–)	35	32	3.5	2.7	ns			
Argmax (grad. norm) (%)	–	[38.2 51.1]	[21.0 30.5]	0.83	<33	87 (+)	79 (–)	83	0.83	86	80	82	39	37	9.0	6.3	4.3			
SVM model	–	–	–	–	–	–	–	–	0.91	85	88	86 (+)	42	38	10.1	8.4	5.5			

† : all $p \leq 0.001$ vs normal

(–): significantly lower and (+): significantly higher than composite SUVr

*: all $p \leq 0.001$ except a: $p \leq 0.01$; b: $p \leq 0.05$; and ns: not significant

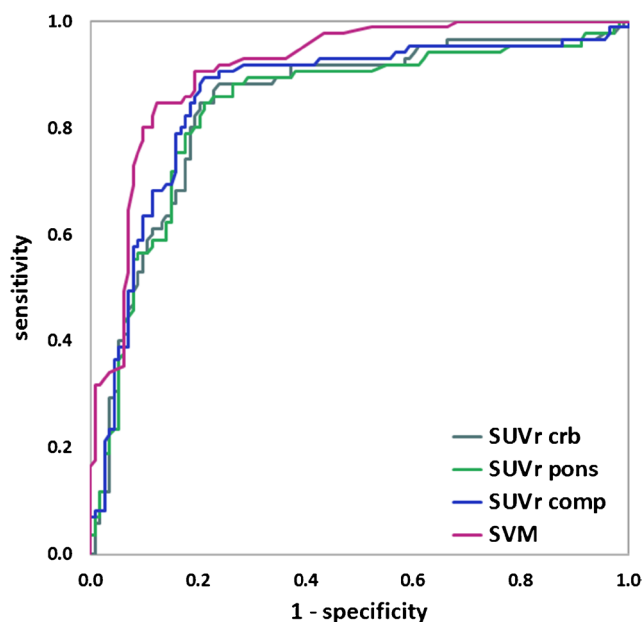


Fig. 4 ROC curves of cerebellar (crb), pontine (pons) and composite (comp) SUVr, and SVM classifier for predicting AD conversion in the longitudinal cohort

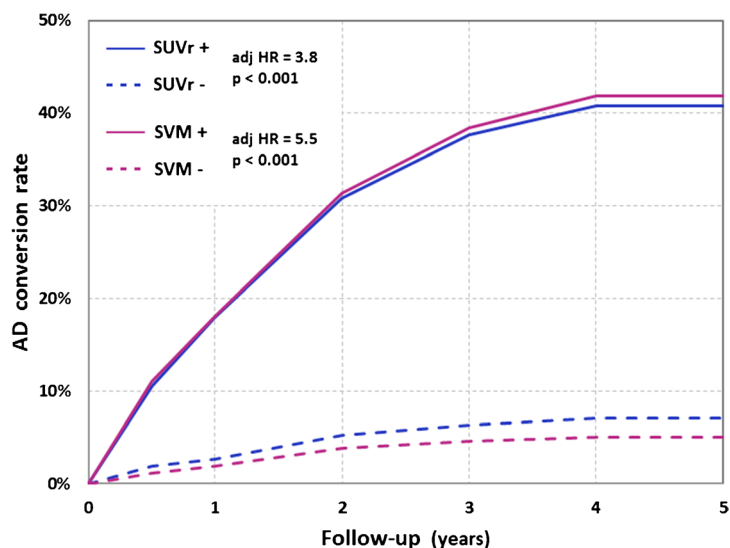
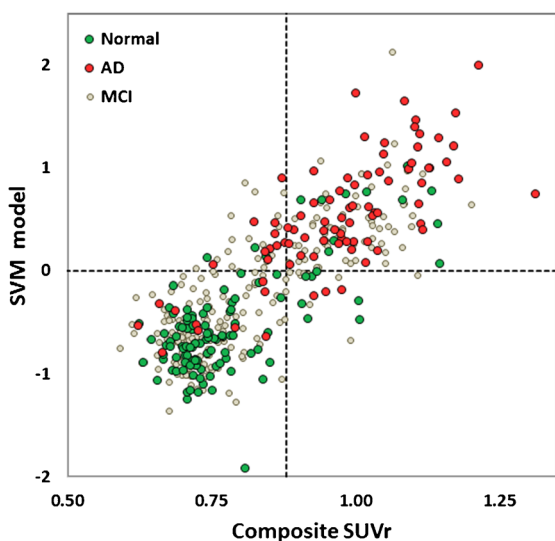


Fig. 5 Predictive value of composite SUVr and the SVM model in the longitudinal cohort. *Left:* Scatter plot of SUVr values and SVM scores according to last known status. The dashed lines indicate the cutoff values for SUVr (0.88) and SVM (0). *Right:* Kaplan–Meier

et al. 2012; Padilla et al. 2012; Dukart et al. 2013). This study demonstrates that, when optimally combined, textural and shape features yield at least as good predictive accuracy as classical semi-quantitation using SUVr. Of note, adding the SUVr to the SVM model did not improve its overall performance, attesting that the chosen SVM parameters were self-consistent descriptors of amyloid deposition and independent predictors of AD conversion. Further improvement of the proposed model is ongoing and should include combining additional biomarkers (MR morphometry, ^{18}F FDG PET, CSF markers), training the model based on autopsy records, and long-term follow-up of the ADNI-2 cohort.

Conclusion

In this study, we demonstrated that textural and shape analysis of florbetapir images provide relevant diagnostic and prognostic information. Combining appropriately chosen textural and shape features yields a predictive model of AD conversion in cognitively impaired subjects that compares

data sets. Yet, implementation of such automated computerized methods in clinical routine requires careful preliminary investigation and validation. SVM and similar classification methods based on PET and/or MR data have already been proved useful for diagnosis and prognosis purposes in MCI and AD patients (Westman

to classical SUVr rating in terms of predictive accuracy. The approach is innovative and appealing in so far as it does not require the segmentation of small cortical ROIs or impose the choice of a subcortical reference. Further investigations are needed to evaluate the robustness of optimal

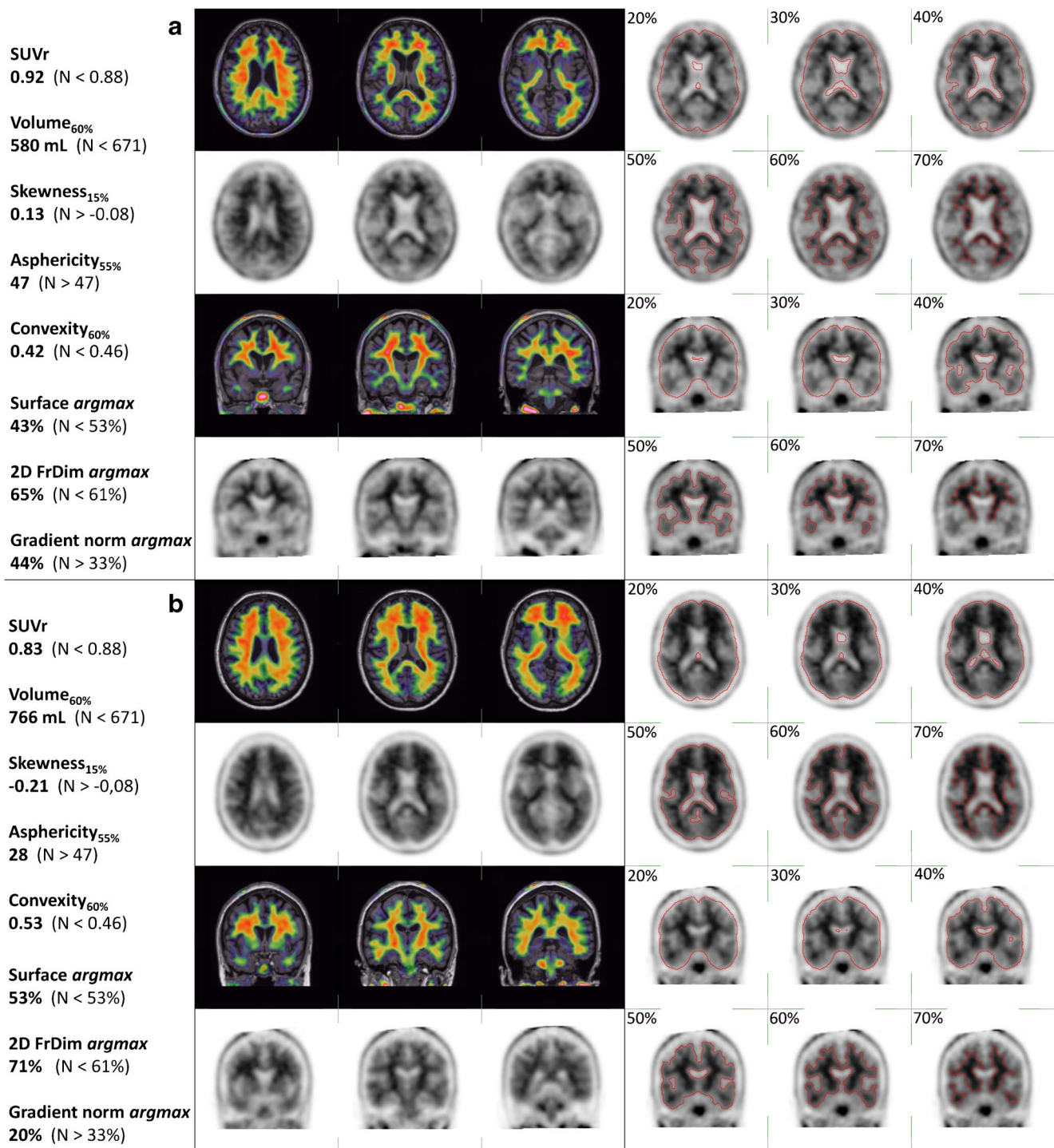


Fig. 6 Two examples from the longitudinal cohort. A: 66-year-old female subject with significant memory concern at baseline who was rated normal after a 36-month follow-up. Composite SUVR was pathological at 0.92. B: 57-year-old female subject with late MCI at baseline who converted to AD after a 24-month follow-up. Composite SUVR was normal at 0.83. Both subjects were correctly classified

using support vector machine. Composite SUVR and relevant textural and shape features are detailed on the left of each panel, along with the normalcy cutoffs established by ROC analysis of the cross-sectional cohort. On the right are detailed the limits of the cerebral VOIs corresponding to segmentation thresholds ranging from 20 to 70%

segmentation thresholds and cutoff values when using other amyloid tracers and according to image resolution. Exploiting additional well-established biomarkers of AD might help improve the performance of the model.

Acknowledgements Data collection and sharing for this project was funded by the Alzheimer's Disease Neuroimaging Initiative (ADNI) (National Institutes of Health Grant U01 AG024904) and DOD ADNI (Department of Defense award number W81XWH-12-2-0012). ADNI is funded by the National Institute on Aging, the National Institute of Biomedical Imaging and Bioengineering, and through generous contributions from the following: AbbVie, Alzheimer's Association; Alzheimer's Drug Discovery Foundation; Araclon Biotech; BioClinica, Inc.; Biogen; Bristol-Myers Squibb Company; CereSpir, Inc.; Cogstate; Eisai Inc.; Elan Pharmaceuticals, Inc.; Eli Lilly and Company; EuroImmun; F. Hoffmann-La Roche Ltd and its affiliated company Genentech, Inc.; Fujirebio; GE Healthcare; IXICO Ltd.; Janssen Alzheimer Immunotherapy Research & Development, LLC.; Johnson & Johnson Pharmaceutical Research & Development LLC.; Lumosity; Lundbeck; Merck & Co., Inc.; Meso Scale Diagnostics, LLC.; NeuroRx Research; Neurotrack Technologies; Novartis Pharmaceuticals Corporation; Pfizer Inc.; Piramal Imaging; Servier; Takeda Pharmaceutical Company; and Transition Therapeutics. The Canadian Institutes of Health Research is providing funds to support ADNI clinical sites in Canada. Private sector contributions are facilitated by the Foundation for the National Institutes of Health (<http://www.fnih.org>). The grantee organization is the Northern California Institute for Research and Education, and the study is coordinated by the Alzheimer's Therapeutic Research Institute at the University of Southern California. ADNI data are disseminated by the Laboratory for Neuro Imaging at the University of Southern California.

Data used in preparation of this paper were obtained from the Alzheimer's Disease Neuroimaging Initiative (ADNI) database (<http://adni.loni.usc.edu/>). As such, the investigators within the ADNI contributed to the design and implementation of ADNI and/or provided data but did not participate in analysis or writing of this paper. A complete listing of ADNI investigators can be found at http://adni.loni.usc.edu/wp-content/uploads/how_to_apply/ADNI_Acknowledgement_List.pdf.

Compliance with ethical standards

Conflict of interest the authors have no conflict of interest to disclose.

Ethical approval All procedures performed in this study were in accordance with the ethical standards of the institutional and/or national research committee and with the 1964 Helsinki declaration and its later amendments or comparable ethical standards.

Informed consent Informed consent was obtained from all individual participants included in the study.

References

- Akamatsu, G., Ikari, Y., Ohnishi, A., Nishida, H., Aita, K., Sasaki, M., Yamamoto, Y., Sasaki, M., & Senda, M. (2016). Automated PET-only quantification of amyloid deposition with adaptive template and empirically pre-defined ROI. *Physics in Medicine and Biology*, *61*, 5768–5780.
- Apostolova, I., Ego, K., Steffen, I. G., Buchert, R., Wertzel, H., Achenbach, H. J., Riedel, S., Schreiber, J., Schultz, M., Furth, C., Derlin, T., Amthauer, H., Hofheinz, F., & Kalinski, T. (2016). The asphericity of the metabolic tumour volume in NSCLC: correlation with histopathology and molecular markers. *European Journal of Nuclear Medicine and Molecular Imaging*, *43*, 2360–2373.
- Ben Bouallègue, F., Al Tabaa, Y., Kafrouni, M., Cartron, G., Vauchot, F., & Mariano-Goulart, D. (2017). Association between textural and morphological tumor indices on baseline PET-CT and early metabolic response on interim PET-CT in bulky malignant lymphomas. *Med Phys* [Epub ahead of print].
- Ben Bouallègue, F., Mariano-Goulart, D., & Payoux, P. Alzheimer's Disease Neuroimaging Initiative (2017): Comparison of CSF markers and semi-quantitative amyloid PET in Alzheimer's disease diagnosis and in cognitive impairment prognosis using the ADNI-2 database. *Alzheimer's Research & Therapy* *9*(1):32.
- Boccardi, M., Altomare, D., Ferrari, C., Festari, C., Guerra, U. P., Paghera, B., Pizzocaro, C., Lussignoli, G., Geroldi, C., Zanetti, O., Cotelli, M. S., Turla, M., Borroni, B., Rozzini, L., Mirabile, D., Defanti, C., Gennuso, M., Prella, A., Gentile, S., Morandi, A., Vollaro, S., Volta, G. D., Bianchetti, A., Conti, M. Z., Cappuccino, M., Carbone, P., Bellandi, D., Abruzzi, L., Bettoni, L., Villani, D., Raimondi, M. C., Lanari, A., Ciccone, A., Facchi, E., Di Fazio, I., Rozzini, R., Boffelli, S., Manzoni, L., Salvi, G. P., Cavaliere, S., Belotti, G., Avanzi, S., Pasqualetti, P., Muscio, C., Padovani, A., & Frisoni, G. B. Incremental Diagnostic Value of Amyloid PET With [18F]-Florbetapir (INDIA-FBP) Working Group (2016): Assessment of the Incremental Diagnostic Value of Florbetapir F 18 Imaging in Patients With Cognitive Impairment: The Incremental Diagnostic Value of Amyloid PET With [18F]-Florbetapir (INDIA-FBP) Study. *JAMA Neurology* *73*:1417–1424.
- Brendel, M., Högenauer, M., Delker, A., Sauerbeck, J., Bartenstein, P., Seibyl, J., & Rominger, A. Alzheimer's Disease Neuroimaging Initiative (2015): Improved longitudinal [(18F)-AV45 amyloid PET by white matter reference and VOI-based partial volume effect correction. *Neuroimage* *108*:450–459.
- Buvat, I., Orihac, F., & Soussan, M. (2015). Tumor Texture Analysis in PET: Where Do We Stand? *Nuclear Medicine*, *56*, 1642–1644.
- Chen, K., Roontiva, A., Thiyyagura, P., Lee, W., Liu, X., Ayutyanont, N., Protas, H., Luo, J. L., Bauer, R., Reschke, C., Bandy, D., Koeppe, R. A., Fleisher, A. S., Caselli, R. J., Landau, S., Jagust, W. J., Weiner, M. W., & Reiman, E. M. Alzheimer's Disease Neuroimaging Initiative (2015): Improved power for characterizing longitudinal amyloid- β PET changes and evaluating amyloid-modifying treatments with a cerebral white matter reference region. *Journal of Nuclear Medicine* *56*:560–566.
- Chicklore, S., Goh, V., Siddique, M., Roy, A., Marsden, P. K., & Cook, G. J. R. (2013). Quantifying tumour heterogeneity in 18F-FDG PET/CT imaging by texture analysis. *European Journal of Nuclear Medicine and Molecular Imaging*, *40*, 133–140.
- Chincarini, A., Sensi, F., Rei, L., Bossert, I., Morbelli, S., Guerra, U. P., Frisoni, G., Padovani, A., & Nobili, F. Alzheimer's Disease Neuroimaging Initiative (2016): Standardized Uptake Value Ratio-Independent Evaluation of Brain Amyloidosis. *Journal of Alzheimer's Disease* *54*:1437–1457.
- Clark, C. M., Pontecorvo, M. J., Beach, T. G., Bedell, B. J., Coleman, R. E., Doraiswamy, P. M., Fleisher, A. S., Reiman, E. M., Sabbagh, M. N., Sadowsky, C. H., Schneider, J. A., Arora, A., Carpenter, A. P., Flitter, M. L., Joshi, A. D., Krautkramer, M. J., Lu, M., Mintun, M. A., & Skovronsky, D. M. AV-45-A16 Study Group (2012): Cerebral PET with florbetapir compared with neuropathology at autopsy for detection of neuritic amyloid- β plaques: a prospective cohort study. *Lancet Neurol* *11*:669–678.
- Doraiswamy, P. M., Sperling, R. A., Johnson, K., Reiman, E. M., Wong, T. Z., Sabbagh, M. N., Sadowsky, C. H., Fleisher, A. S., Carpenter, A., Joshi, A. D., Lu, M., Grundman, M., Mintun, M. A., Skovronsky, D. M., & Pontecorvo, M. J. AV45-A11 Study Group, AV45-A11 Study Group (2014): Florbetapir F 18 amyloid

- PET and 36-month cognitive decline: a prospective multicenter study. *Molecular Psychiatry* 19:1044–1051.
- Dubois, B., Feldman, H. H., Jacova, C., Dekosky, S. T., Barberger-Gateau, P., Cummings, J., Delacourte, A., Galasko, D., Gauthier, S., Jicha, G., Meguro, K., O'Brien, J., Pasquier, F., Robert, P., Rossor, M., Salloway, S., Stern, Y., Visser, P. J., & Scheltens, P. (2007). Research criteria for the diagnosis of Alzheimer's disease: revising the NINCDS-ADRDA criteria. *Lancet Neurology*, 6, 734–746.
- Dukart, J., Mueller, K., Barthel, H., Villringer, A., Sabri, O., & Schroeter, M. L. Alzheimer's Disease Neuroimaging Initiative (2013): Meta-analysis based SVM classification enables accurate detection of Alzheimer's disease across different clinical centers using FDG-PET and MRI. *Psychiatry Research* 212:230–236.
- El Naqa, I., Grigsby, P., Apte, A., Kidd, E., Donnelly, E., Khullar, D., Chaudhari, S., Yang, D., Schmitt, M., Laforest, R., Thorstad, W., & Deasy, J. O. (2009). Exploring feature-based approaches in PET images for predicting cancer treatment outcomes. *Pattern Recognition*, 42, 1162–1171.
- Ellendt, S., Voß, B., Kohn, N., Wagels, L., Goerlich, K., Drexler, E., Schneider, F., & Habel, U. (2016). Predicting stability of Mild Cognitive Impairment (MCI): findings of a community based sample. *Curr Alzheimer Res.*
- Falconer, K. 1990. Fractal geometry: mathematical foundations and applications. John Wiley.
- Goh, V., Sanghera, B., Wellsted, D. M., Sundin, J., & Halligan, S. (2009). Assessment of the spatial pattern of colorectal tumour perfusion estimated at perfusion CT using two-dimensional fractal analysis. *European Radiology*, 19, 1358–1365.
- Gonzalez-Escamilla, G., Lange, C., Teipel, S., Buchert, R., & Grothe, M. J. Alzheimer's Disease Neuroimaging Initiative (2017): PET-PVE12: an SPM toolbox for Partial Volume Effects correction in brain PET - Application to amyloid imaging with AV45-PET. *Neuroimage* 147:669–677.
- Haralick, R. M., Shanmugam, K., & Dinstein, I. (1973). Textural features for image classification. *IEEE Transactions on Systems, Man, and Cybernetics*, 3, 610–621.
- Hayano, K., Lee, S. H., Yoshida, H., Zhu, A. X., & Sahani, D. V. (2014). Fractal analysis of CT perfusion images for evaluation of antiangiogenic treatment and survival in hepatocellular carcinoma. *Academic Radiology*, 21, 654–660.
- Hsiao, I. T., Huang, C. C., Hsieh, C. J., Wey, S. P., Kung, M. P., Yen, T. C., & Lin, K. J. (2013). Perfusion-like template and standardized normalization-based brain image analysis using 18F-florbetapir (AV-45/Amyvid) PET. *European Journal of Nuclear Medicine and Molecular Imaging*, 40, 908–920.
- Jack, C. R., Knopman, D. S., Jagust, W. J., Shaw, L. M., Aisen, P. S., Weiner, M. W., Petersen, R. C., & Trojanowski, J. Q. (2010). Hypothetical model of dynamic biomarkers of the Alzheimer's pathological cascade. *Lancet Neurology*, 9, 119–128.
- Joshi, A., Koeppe, R. A., & Fessler, J. A. (2009). Reducing between scanner differences in multi-center PET studies. *Neuroimage*, 46, 154–159.
- Joshi, A. D., Pontecorvo, M. J., Clark, C. M., Carpenter, A. P., Jennings, D. L., Sadowsky, C. H., Adler, L. P., Kovnat, K. D., Seibyl, J. P., Arora, A., Saha, K., Burns, J. D., Lowrey, M. J., Mintun, M. A., & Skovronsky, D. M. Florbetapir F 18 Study Investigators (2012): Performance characteristics of amyloid PET with florbetapir F 18 in patients with Alzheimer's disease and cognitively normal subjects. *Journal of Nuclear Medicine* 53:378–384.
- Joshi, A. D., Pontecorvo, M. J., Lu, M., Skovronsky, D. M., Mintun, M. A., & Devous, M. D. (2015). A Semiautomated Method for Quantification of F 18 Florbetapir PET Images. *Journal of Nuclear Medicine*, 56, 1736–1741.
- klunk, W. E., Koeppe, R. A., Price, J. C., Benzinger, T. L., Devous, M. D., Jagust, W. J., Johnson, K. A., Mathis, C. A., Minhas, D., Pontecorvo, M. J., Rowe, C. C., Skovronsky, D. M., & Mintun, M. A. (2015). The Centiloid Project: standardizing quantitative amyloid plaque estimation by PET. *Alzheimers Dement*, 11, 1-15-4.
- Klyuzhin, I. S., Blinder, S., Mabrouk, R., Rahmim, A., & Sossi, V. (2015): Investigation of texture quantification parameters for neurological PET image analysis. IEEE Nuclear Science Symposium and Medical Imaging Conference.
- Lambin, P., Rios-Velazquez, E., Leijenaar, R., Carvalho, S., van Stiphout, R. G. P. M., Granton, P., Zegers, C. M. L., Gillies, R., Boellard, R., Dekker, A., & Aerts, H. J. W. L. (2012). Radiomics: extracting more information from medical images using advanced feature analysis. *European Journal of Cancer*, 48, 441–446.
- Landau, S. M., Fero, A., Baker, S. L., Koeppe, R., Mintun, M., Chen, K., Reiman, E. M., & Jagust, W. J. (2015). Measurement of longitudinal β -amyloid change with 18F-florbetapir PET and standardized uptake value ratios. *Journal of Nuclear Medicine*, 56, 567–574.
- Landau, S. M., Mintun, M. A., Joshi, A. D., Koeppe, R. A., Petersen, R. C., Aisen, P. S., Weiner, M. W., & Jagust, W. J. Alzheimer's Disease Neuroimaging Initiative (2012): Amyloid deposition, hypometabolism, and longitudinal cognitive decline. *Annals of Neurology* 72:578–586.
- McKhann, G., Drachman, D., Folstein, M., Katzman, R., Price, D., & Stadlan, E. M. (1984). Clinical diagnosis of Alzheimer's disease: report of the NINCDS-ADRDA Work Group under the auspices of Department of Health and Human Services Task Force on Alzheimer's Disease. *Neurology*, 34, 939–944.
- Minoshima, S., Drzezga, A. E., Barthel, H., Bohnen, N., Djekidel, M., Lewis, D. H., Mathis, C. A., McConathy, J., Nordberg, A., Sabri, O., Seibyl, J. P., Stokes, M. K., & Van Laere, K. (2016). SNMMI Procedure Standard/EANM Practice Guideline for Amyloid PET Imaging of the Brain 1.0. *Journal of Nuclear Medicine*, 57, 1316–1322.
- Miwa, K., Inubushi, M., Wagatsuma, K., Nagao, M., Murata, T., Koyama, M., Koizumi, M., & Sasaki, M. (2014). FDG uptake heterogeneity evaluated by fractal analysis improves the differential diagnosis of pulmonary nodules. *European Journal of Radiology*, 83, 715–719.
- Nemmi, F., Saint-Aubert, L., Adel, D., Salabert, A.-S., Pariente, J., Barbeau, E. J., Payoux, P., & Péran, P. (2014). Insight on AV-45 binding in white and grey matter from histogram analysis: a study on early Alzheimer's disease patients and healthy subjects. *European Journal of Nuclear Medicine and Molecular Imaging*, 41, 1408–1418.
- Ong, K. T., Villemagne, V. L., Bahar-Fuchs, A., Lamb, F., Langdon, N., Catafau, A. M., Stephens, A. W., Seibyl, J., Dinkelborg, L. M., Reiningner, C. B., Putz, B., Rohde, B., Masters, C. L., & Rowe, C. C. (2015). $A\beta$ imaging with 18F-florbetaben in prodromal Alzheimer's disease: a prospective outcome study. *Journal of Neurology, Neurosurgery, and Psychiatry*, 86, 431–436.
- Orlhac, F., Thézé, B., Soussan, M., Boisgard, R., & Buvat, I. (2016). Multiscale Texture Analysis: From 18F-FDG PET Images to Histologic Images. *Journal of Nuclear Medicine*, 57, 1823–1828.
- Padilla, P., López, M., Górriz, J. M., Ramírez, J., Salas-González, D., & Álvarez, I. Alzheimer's Disease Neuroimaging Initiative (2012): NMF-SVM based CAD tool applied to functional brain images for the diagnosis of Alzheimer's disease. *IEEE Transactions on Medical Imaging* 31:207–216.
- Petersen, R. C., Aisen, P., Boeve, B. F., Geda, Y. E., Ivnik, R. J., Knopman, D. S., Mielke, M., Pankratz, V. S., Roberts, R., Rocca, W. A., Weigand, S., Weiner, M., Wiste, H., & Jack, C. R. (2013). Mild cognitive impairment due to Alzheimer disease in the community. *Ann Neurol*, 74, 199–208.
- Petersen, R. C., Aisen, P. S., Beckett, L. A., Donohue, M. C., Gamst, A. C., Harvey, D. J., Jack, C. R., Jagust, W. J., Shaw, L. M., Toga, A. W., Trojanowski, J. Q., & Weiner, M. W. (2010). Alzheimer's

- Disease Neuroimaging Initiative (ADNI): clinical characterization. *Neurology*, 74, 201–209.
- Pontecorvo, M. J., & Mintun, M. A. (2011). PET amyloid imaging as a tool for early diagnosis and identifying patients at risk for progression to Alzheimer's disease. *Alzheimer's Research & Therapy*, 3, 11.
- Rullmann, M., Dukart, J., Hoffmann, K.-T., Luthardt, J., Tjepolt, S., Patt, M., Gertz, H.-J., Schroeter, M. L., Seibyl, J., Schulz-Schaeffer, W. J., Sabri, O., & Barthel, H. (2016). Partial-Volume Effect Correction Improves Quantitative Analysis of 18F-Florbetaben β -Amyloid PET Scans. *Journal of Nuclear Medicine*, 57, 198–203.
- Saint-Aubert, L., Nemmi, F., Péran, P., Barbeau, E. J., Payoux, P., Chollet, F., & Pariente, J. (2014). Comparison between PET template-based method and MRI-based method for cortical quantification of florbetapir (AV-45) uptake in vivo. *European Journal of Nuclear Medicine and Molecular Imaging*, 41, 836–843.
- Schreiber, S., Landau, S. M., Fero, A., Schreiber, F., & Jagust, W. J. Alzheimer's Disease Neuroimaging Initiative (2015): Comparison of Visual and Quantitative Florbetapir F 18 Positron Emission Tomography Analysis in Predicting Mild Cognitive Impairment Outcomes. *JAMA Neurology* 72:1183–1190.
- Schwarz, C. G., Senjem, M. L., Gunter, J. L., Tosakulwong, N., Weigand, S. D., Kemp, B. J., Sychalla, A. J., Vemuri, P., Petersen, R. C., Lowe, V. J., & Jack, C. R. (2017). Optimizing PiB-PET SUVR change-over-time measurement by a large-scale analysis of longitudinal reliability, plausibility, separability, and correlation with MMSE. *Neuroimage*, 144, 113–127.
- Shokouhi, S., Mckay, J. W., Baker, S. L., Kang, H., Brill, A. B., Gwirtsman, H. E., Riddle, W. R., Claassen, D. O., & Rogers, B. P. Alzheimer's Disease Neuroimaging Initiative (2016): Reference tissue normalization in longitudinal (18)F-florbetapir positron emission tomography of late mild cognitive impairment. *Alzheimer's Research & Therapy* 8:2.
- Shokouhi, S., Rogers, B. P., Kang, H., Ding, Z., Claassen, D. O., Mckay, J. W., & Riddle, W. R. Alzheimer's Disease Neuroimaging Initiative (2015): Modeling clustered activity increase in amyloid-beta positron emission tomographic images with statistical descriptors. *Clinical Interventions in Aging* 10:759–770.
- Smitha, K. A., Gupta, A. K., & Jayasree, R. S. (2015). Fractal analysis: fractal dimension and lacunarity from MR images for differentiating the grades of glioma. *Physics in Medicine and Biology*, 60, 6937–6947.
- Vapnik, V. N. (1999). An overview of statistical learning theory. *IEEE Transactions on Neural Networks*, 10, 988–999.
- Westman, E., Muehlboeck, J.-S., & Simmons, A. (2012). Combining MRI and CSF measures for classification of Alzheimer's disease and prediction of mild cognitive impairment conversion. *Neuroimage*, 62, 229–238.